



Tracking the corrosion of magnesium sand cast AM50 alloy in chloride environments

R. Matthew Asmussen^a, Pellumb Jakupi^a, Mohsen Danaie^b, Gianluigi A. Botton^b, David W. Shoesmith^{a,*}

^a Department of Chemistry and Surface Science Western, Western University, London, Ontario N5A 6B7, Canada

^b Department of Materials Science and Engineering, Brockhouse Institute for Materials Research and Canadian Centre for Electron Microscopy, McMaster University, Hamilton, Ontario, Canada

ARTICLE INFO

Article history:

Received 3 February 2013

Accepted 28 May 2013

Available online 7 June 2013

Keywords:

A. Magnesium

A. Alloy

B. SEM

B. TEM

Confocal laser scanning microscopy

ABSTRACT

An experimental procedure for tracking corrosion on lightweight alloys has been developed using a combination of microscopy and corrosion studies using commercial sand cast magnesium AM50 alloys. Corrosion penetration depths were measured and characterized with CLSM and SEM/XEDS, respectively. Corrosion depths on α -grains in the alloys were expressed as a function of their Al content. Al-rich β -phases and eutectic α -phase microstructures were observed to be most corrosion resistant due to an enrichment of Al, identified with TEM, near the oxide/alloy interface. Sand cast alloys were found to be susceptible to major corrosion events in regions with depleted Al content.

© 2013 Elsevier Ltd. All rights reserved.

1. Introduction

Magnesium alloys are attractive materials for industrial application due to their high strength-to-weight ratio. However, a major deficiency is their inadequate corrosion resistance when exposed to aqueous and humid environments exemplified by those encountered in automotive applications [1–3]. As the most electrochemically active structural material, Mg, when placed in electrical contact with a dissimilar metal/alloy in an aqueous medium can establish an active galvanic couple resulting in anodic polarization and corrosion of Mg and consequently the generation of very high current densities and corrosion rates [4].

AM50, a commercial Mg alloy, is used for its exceptional castability [5,6]. The major microstructural constituents of AM50 are: a Mg-rich α -phase, an Al-enriched eutectic α -phase containing β -phase (Mg₁₇Al₁₂), and Al–Mn intermetallics [7,8]. As Mg alloys freely undergo corrosion in aqueous environments due their position in the electrochemical series, the effect of the microstructure on this corrosion process must be understood. Following the study of grain size on pure Mg by Birbilis [9] which concluded other factors may override the corrosion effects of grain size on pure Mg, the effect of grain size on the corrosion of other alloys including AZ31 [10–12], ZK60 [13] and AZ91 [14–16] However, presently no agreement on whether a decrease in grain size dampens or

accelerates corrosion of the alloys exists [17]. With changing microstructure the size the distribution of secondary microstructures, which can serve as local cathodes, is also altered. Previous macroscale studies on AM50 and other Mg alloys suggest microgalvanic coupling can occur between the β -phase and/or intermetallics and the α -phase, thus, accelerating the corrosion of the Mg rich α -phase [18–20]. Both β -phase and the AlMn intermetallics are known to be cathodic to the Mg matrix, with the strongest cathode being the AlMn intermetallics in aqueous environments [11]. The distribution of β -phase has been suggested to affect the corrosion of Mg AZ91 alloys [21–23]. The aim of this study is to track the location of corrosion initiation and to quantify the extent of propagation (as a penetration depth) on sand cast AM50 alloys based on microstructural characteristics; specifically, the varying Al-content of α -grains and the proximity of β -phase networks. Due to the variable Al-content of α -grains [20] it is possible to have individual grains with different corrosion rates.

Alloying Mg with Al has been shown to alter the microstructure [24], and significantly influence corrosion resistance [3,25–27]. While corrosion resistance is usually assessed in terms of the bulk Al content of the alloy this study assesses corrosion damage as a function of the Al content of individual α -grains and its distribution throughout the sample. With alteration in microstructure size and distribution, this can be viewed as changing the distribution of the Al throughout the alloy. In this study, corrosion damage is quantified using confocal laser scanning microscopy (CLSM), a technique previously shown to quantify damage on Mg alloys and coatings [28,29] and on other materials [30,31]. The chemical

* Corresponding author. Address: Western University, 1161 Richmond St., London, Ontario N6A 5B7, Canada. Tel.: +1 519 661 2111x86366.

E-mail address: dwshoesm@uwo.ca (D.W. Shoesmith).

content and morphology of sub-surface corroded and un-corroded regions were also investigated by forming cross-sections using a focused-ion beam (FIB), followed by chemical analysis using X-ray energy dispersive spectroscopy (XEDS) and transmission electron microscopy (TEM). The surface and sub-surface chemistry of microstructural features was compared to their corrosion rate and damage morphology to determine which microstructural features enhance or repress corrosion resistance.

2. Experimental procedures

2.1. Sample preparation

As-received AM50 sand cast rods were machined into $1 \times 1 \times 0.7$ cm electrodes. One side (1 cm^2) was tapped to accommodate a threaded rod to allow electrical connection to external circuitry. The 1 cm^2 side to be examined was pre-treated using the following procedure: The sample was ground successively up to 4000 SiC grit. A thin layer of paraffin wax was applied to each SiC pad to maintain the integrity of the pad and to provide an additional lubricant. An equal volume mixture of ethanol and propanol was used as a lubricant on the SiC pad. The ground alloy surface was then polished on a Struers DP-Dur cloth saturated in $3 \mu\text{m}$ Struers DP-Suspension A for 5–10 min with the ethanol/propanol mixture once again used as a lubricant. The final stage consisted of polishing, for 2–3 min, on a Struers OP-Chem cloth using an equal volume mixture of Struers OP-S Suspension and ethylene glycol, as an abrasive. The polished sample was rinsed and sonicated in anhydrous ethanol for 2 min, air dried, and then stored in a desiccator.

2.2. Instrumentation

AM50 electron micrographs were collected in back-scattered and secondary electron modes using a LEO 440 SEM, Hitachi 3400-N Variable Pressure SEM and a Hitachi 4500-N equipped with a Quartz One XEDS System to determine elemental concentrations of α -grains and other microstructural components.

Depth profiles on un-corroded and corroded surfaces were measured by detecting the reflected light intensity from a Zeiss 510 confocal, HeNe 633 nm laser. The polished sample surface was placed downward, suspended by a stage, facing an inverted objective. Light intensities were normalized into a depth profile by considering how many steps of known distance (slices) through the focal plane, in the z -direction, are required to reach the deepest region on the sample surface. The differences in light intensities were then converted to a distance. At depths of $>30 \mu\text{m}$, the limit of clear image resolution is reached.

2.3. Tracking corrosion on the microscale

Prior to corrosion experiments, the polished surface was analyzed by SEM/XEDS and confocal laser scanning microscopy (CLSM). The co-ordinates of an area of interest (AOI) were recorded (relative to a surface edge) so that the same area ($275 \mu\text{m} \times 450 \mu\text{m}$) could be subsequently located after intermittent immersions. All experiments were performed in a naturally aerated 1.6 wt% NaCl (reagent grade, 99% assay) solution prepared with MilliQ® water ($18 \text{ M}\Omega \text{ cm}$) at ambient temperature ($\sim 22.5^\circ\text{C}$). The polished side of the AM50 electrode was immersed in the electrolyte and suspended from a stainless steel rod with the electrolyte level located approximately 1–2 mm above the polished surface.

After immersion in the chloride solution, the corroded surface was rinsed and sonicated in anhydrous ethanol, and dried. The

corroded AOI was then analyzed using SEM/XEDS and CLSM, and compared to the same location prior to corrosion. This procedure was repeated after each of a series of immersions, which simulate wet–dry cycling, to determine the evolution of damage morphology and penetration depth with time. On completion of immersion experiments (after a total of 96 h immersion), the sample was further analyzed with FIB (Zeiss NVision 40) for imaging and site-specific sample preparation for TEM using a FEI Titan 80-300 (scanning) transmission electron microscope ((S)TEM) equipped with an X-ray energy-dispersive spectrometer (XEDS – Oxford Inca, Si(Li) detector) For XEDS data analysis commercial software INCA (Oxford Instruments) was used.

2.4. Surface montage imaging

A square 16 mm^2 sand cast sample of 2 mm thickness was mounted in Struers EpoFix™ epoxy so that only a 16 mm^2 surface was exposed. The surface was ground and polished as described in Section 2.1. A total of 60 images, at $150\times$ magnification, were recorded across the entire 16 mm^2 polished surface using a Hitachi SU6600 Field Emission SEM. The images were then stitched using Image-Pro Plus 7.0® into a 10×6 grid to yield a final image map of the entire 16 mm^2 surface. The sample was then immersed in chloride solution and corrosion analyses performed after a sequence of immersions as described in Section 2.3. Between each immersion the surface was analyzed by SEM as described.

3. Results

3.1. Corrosion behavior of sand cast AM50 alloys in 1.6 wt% NaCl

Fig. 1 displays an SEM micrograph of a selected AOI (Fig. 1a) and the corresponding XEDS maps for Mg (Fig. 1b), Al (Fig. 1c) and Mn (Fig. 1d). This area exhibits an Al-rich network of eutectic α -phase interlaced with β -phase mainly in the centre of the AOI. The presence of nine Al–Mn intermetallics can be observed in the AOI. Following initial imaging with SEM and CLSM, the sample was immersed in the 1.6 wt% NaCl solution for a series of 24 h exposure periods. Between each immersion, the AOI is re-located and imaged with SEM and CLSM to monitor corrosion evolution on the surface. The SEM and CLSM light intensity images recorded after each 24 h. immersion period are presented in Fig. 2. The initial polished surface undergoes dramatic changes after only 24 h of immersion mainly near the bottom of the AOI, where several α -grains have corroded. The Al rich regions in the centre appear to be more resistant to corrosion. After 48 h, a significantly corroded area is observed on the left-centre α -grain of the AOI. After 72 h, several other α -grains experienced extensive damage, a process which continues up to 96 h of exposure. Corrosion at the α -grains is directed inward into the alloy and leaves behind a skeletal uncorroded network. The cracking observed on some α -grains may be a result of the accumulated corrosion product drying when the sample is removed from solution and cannot be resolved at the selected magnification by the CLSM due to light scattering at the cracks. This cracking was not a result of the intermittent wet–dry cycling undergone by the sample, as it still occurs with a continuous exposure of 96 h, shown in Fig. 3.

It is clear from Fig. 2 that α -grains undergo preferential attack as expected from previous studies [32], whereas other microstructural constituents of the alloy display a much different behavior. Fig. 4 tracks an “ear-shaped” β -phase centered between two α -grains throughout a full 96 h immersion cycle. After 24 h (Fig. 4a), corrosion product is loosely dispersed over the area, with some change in corrosion depth on the neighboring α -grains evidenced by the darkening in the corners of the image. The corrosion

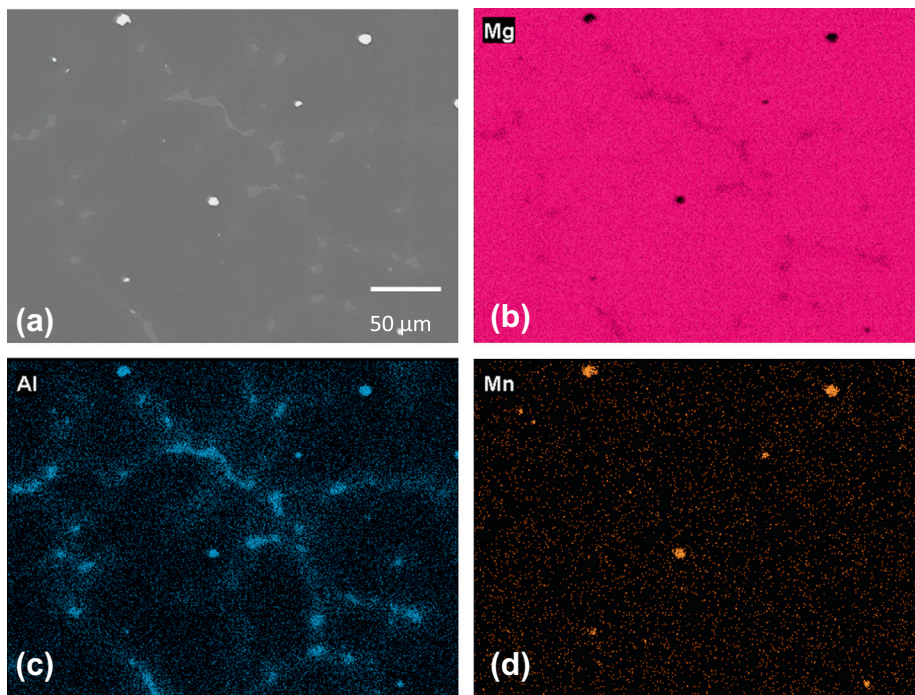


Fig. 1. (a) SEM backscatter (BSE-20 kV) image of a selected area of interest (AOI) on a sand cast AM50 alloy and the corresponding EDX maps for (b) Mg, (c) Al, and (d) Mn.

product layer becomes more pronounced in patches following 48 h of immersion Fig. 4b, with the β -phase being masked by the corrosion product layer. The β -phase can still be distinguished due to a change in the morphology of the corrosion product above the β -phase compared to the surrounding coverage. As the corrosion product continues to accumulate, Fig. 4c (72 h) and Fig. 4d (96 h), the location of the β -phase is more easily resolved in the image. The corrosion product accumulated over the β -phase is more porous than the adjacent areas, but has the same composition [33]. This increased porosity can be induced by cathodic behavior of the β -phase relative to surrounding areas.

The surface morphology of the Al–Mn intermetallics is altered throughout the corrosion process. Fig. 5a shows an Al–Mn intermetallic (contained within an α -grain in the left centre of the image along with its β -phase neighbor) following 24 h of immersion. A dome of corrosion product has accumulated over the intermetallic with the surrounding α -grain showing some corrosion damage, while little corrosion product is present over the β -phase region. This dome structure remains intact throughout 72 h of immersion Fig. 5b and c, while corrosion proceeds on the α -grain. Within the next immersion cycle up to 96 h of immersion Fig. 5d, the dome has collapsed and the formation of a new dome of accumulated corrosion product has commenced over the exposed intermetallic. Hydrogen evolution or delamination of the intermetallic surface could have lead to this collapse. Making up the dome of corrosion product is an outer layer of $\text{Mg}(\text{OH})_2$ and an inner structure of MgO , as determined by electron energy loss spectroscopy and electron diffraction, as described elsewhere [33]. From this work, it has been reported that below this accumulated corrosion product layer there is a delamination of the intermetallic, producing a Mn_3O_4 layer and an absence of Al [33]. These two observations suggest that a localized pH change is occurring at the intermetallics. If the intermetallics are acting as localized cathodes, hydrogen evolution can lead to an increase in pH at such sites. The presence of OH^- can produce the outer layer of $\text{Mg}(\text{OH})_2$ while assisting the dissolution of Al from the intermetallic surface [33]. The dome structures over the intermetallics are evidence of their localized cathodic behavior, although intermetallics free of these domes

are also observed (arrow in Fig. 5d). The absence of a corrosion product dome at the Al–Mn intermetallic suggests no local pH change, and thus inactivity as a cathode at that point in the corrosion process. This trait is not yet fully understood.

3.2. Role of Al in the corrosion of sand cast AM50 alloys

Individual α -grains differ in Al-contents, which can be measured from XEDS data extracted from the maps. α -grain boundaries on the sand cast alloys are not readily defined without etching, which was avoided in order to maintain the natural state of the alloy. In this case, the α -grain boundaries are delineated as regions enclosed by the Al-rich network, as shown in Fig. 6. The Al content of the individual α -grains was obtained using the area trace function of the software, and an average Al content calculated versus the software standard. The average Al values reflect the surface Al-content and sub-surface Al content due to the excitation volume ($\sim 4 \mu\text{m}$) of the electron beam. From the CLSM images and the measured light intensities, corrosion penetration depth profiles of the surface are recorded by linescan analysis. Fig. 7a shows the CLSM linescan region of the AOI from Fig. 2 with the green line identifying the location of the selected linescan used for depth measurement. The depths were calculated from the distance between the highest and lowest light intensities on the AOI. Fig. 7b shows the absolute depth profiles recorded along this linescan after successive periods of immersion up to 72 h. The grey-shaded areas are representative of the β -phase locations encountered in the linescan. As time progressed, corrosion on the α -grains was observed accompanied by an increase in depth.

From a series of linescans, the evolution of the corrosion penetration depths (measured at the centre of the grain) on α -grains as a function of their Al-content, determined by XEDS, for different exposure times are obtained (Fig. 8). The analyses of a statistically relevant number of grains recorded from four different sand cast samples are summarized in a plot of the corrosion penetration depth versus the Al content of α -grains (wt%) over the sequence of immersion periods. This figure shows that grains containing lower amounts of measured Al, generally $<3 \text{ wt}\%$, experienced

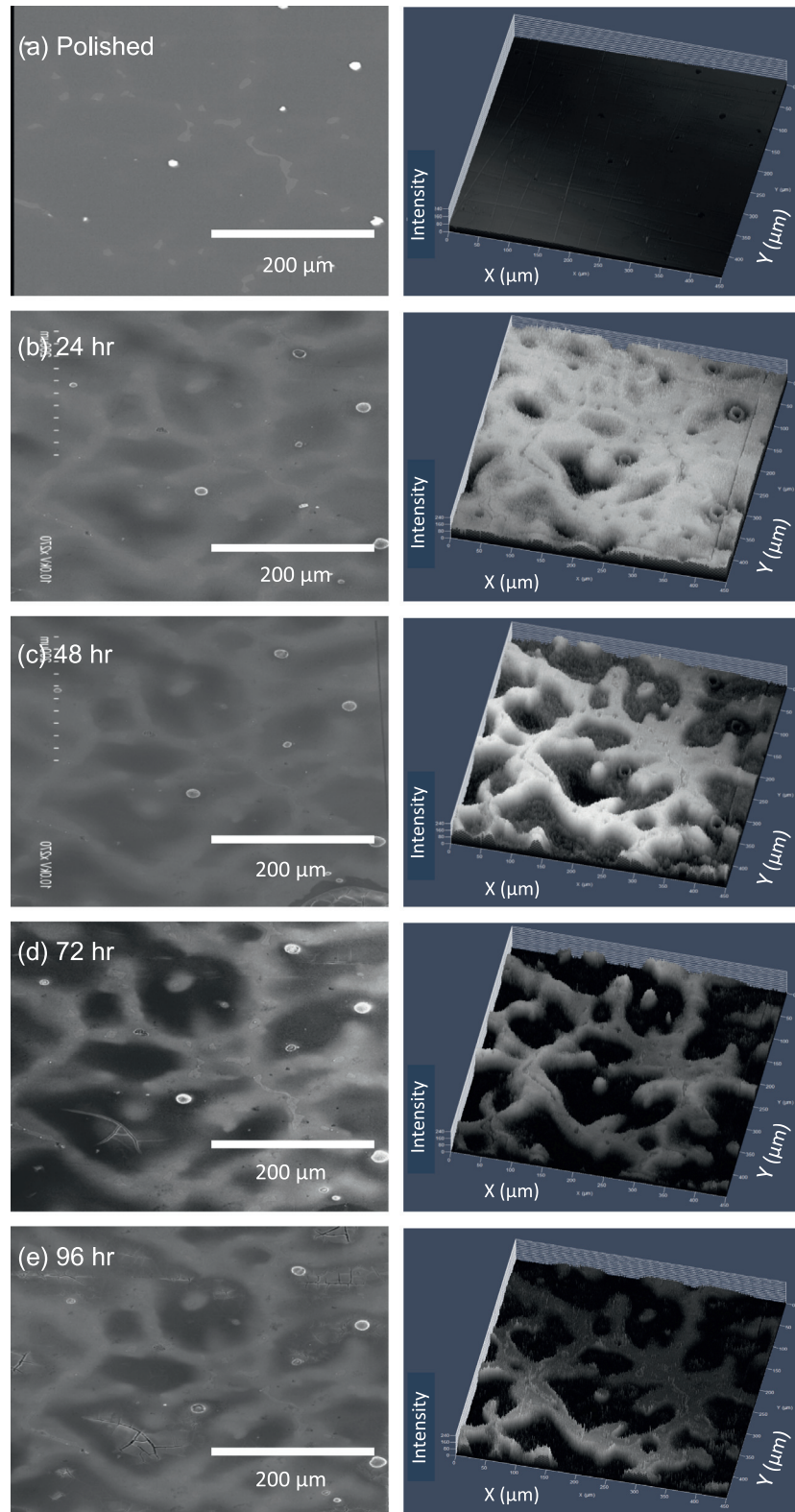


Fig. 2. Secondary electron (SE) SEM (10 kV) and CLSM images of the $450\ \mu\text{m} \times 450\ \mu\text{m}$ AOI on an AM50 sample corroded through successive wet–dry cycles following (a) 0 h, (b) 24 h, (c) 48 h, (d) 72 h and (e) 96 h exposure. The intermetallic marked with an arrow in (a) is displayed in Fig. 5 and CLSM images presented on a light intensity scale 0–240.

higher corrosion penetration to depths approaching $20\ \mu\text{m}$. However, a linear trend does not exist, since grains with nearly identical Al content corroded at different rates, suggesting that neighboring microstructures also influence corrosion rates. The most rapidly

corroding grains, irrespective of Al content, contained Al–Mn inclusions such as the one identified in Fig. 5 (eight of such grains were observed in total), which are known to act as local cathodes [34].

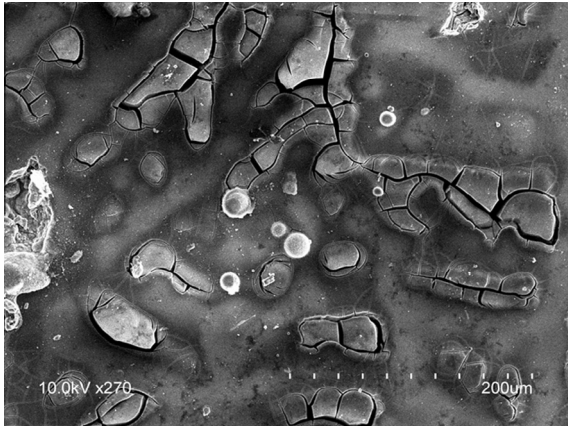


Fig. 3. SEM micrograph (SE-10 kV) of a sand cast corroded surface after 96 h of continuous exposure in 1.6 wt% NaCl.

Both intermetallic and β -phases can serve as cathodes coupled to anodic Mg-rich α -grains. Regions in the direct vicinity of the β -phase (the eutectic α -phase) would, therefore, be expected to be susceptible to corrosion. However, as seen in the CLSM images in Fig. 2, areas near the β -phase are still more resistant to corrosion. The corrosion resistant regions in these samples correspond to the Al-rich network observed in the Al XEDS maps Fig. 1, consistent with other reports on higher corrosion resistant surface regions on Mg alloys [12] possibly due to an Al layer [24,35,36]. Although a detailed analysis of the corrosion product/alloy interface, using high resolution analytical microscopy, is discussed elsewhere [33], a summary of the findings is given here. Following 96 h of immersion, a FIB cross-section Fig. 9a, was cut from the site of a corrosion resistant β -phase region to investigate what feature(s) could be suppressing the corrosion rate at these locations. Prior to cross-sectioning a tungsten strip was deposited on the surface to maintain the integrity of the surface film and prevent damage from the Ga beam. A TEM lamella was removed from this cross section and the areas marked in red and green in Fig. 9b were analyzed following thinning of two electron transparent windows.

For all the XEDS data in TEM Fig. 9c and d, the sample was tilted to $\alpha = +15^\circ$ to enhance the strength of signal. The area labeled with a green frame, containing a β -phase section, was analyzed with XEDS to produce the maps shown in Fig. 9c. An accumulation of Al at the oxide/alloy interface can be seen in the XEDS Al map, lying just beneath the columnar-like corrosion product layer containing oxygen and above the Mg-rich alloy. One possibility is that this Al could be present due to the proximity to the β -phase. However, analysis of an area away from the β -phase (marked in red in Fig. 9b), also shows a surface Al layer, Fig. 9d. Based on the depth profiles shown in Fig. 2, which demonstrate that regions enriched in Al in close proximity to β -phase (i.e., at similar locations to that analyzed in Fig. 9d) are more corrosion resistant compared to α -grains, it is suggested that this Al-layer is largely responsible for the improved corrosion resistance.

3.3. Major corrosion events on sand cast AM50 alloys

Throughout the immersion tests, major corrosion events, characterized by damaged areas over 25 μm in diameter and penetrating upwards of hundreds of microns into the alloy, were commonly observed. These sites are not limited to edge effects on the unmounted samples, and once initiated, corrosion propagation is not limited by any nearby microstructural features, such as Al-enriched regions. A clear example is demonstrated by the annihilation of an AOI Fig. 10a, following 24 h of immersion, Fig. 10b where the AOI is highlighted by the red box.

To investigate the origin of these major corrosion events, the exposed 4 mm \times 4 mm surface of an epoxy mounted sand cast alloy was entirely imaged prior to corrosion, with SEM in backscatter mode. The images were stitched together to produce the montage image shown in Fig. 11a. Following the first 2 h immersion, the surface was again fully mapped, and five major damage sites were observed (marked with arrows), only one of which occurs at the epoxy/sample interface and hence could be attributed to crevice corrosion, Fig. 11b. After 3 h of immersion a 6th major event initiated on the right- to-middle of the sample, Fig. 11c. A further 1 h of immersion leads to the appearance of a 7th major site initiating on the bottom right of the sample.

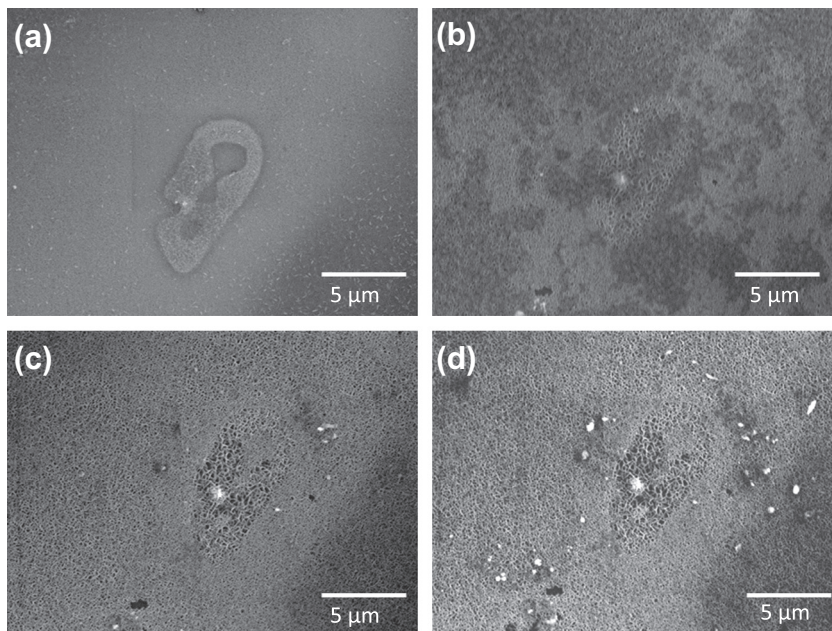


Fig. 4. SEM images (SE-10 kV) showing the progress of corrosion near a β -phase region following (a) 24 h, (b) 48 h, (c) 72 h, and (d) 96 h of immersion in 1.6 wt% NaCl.

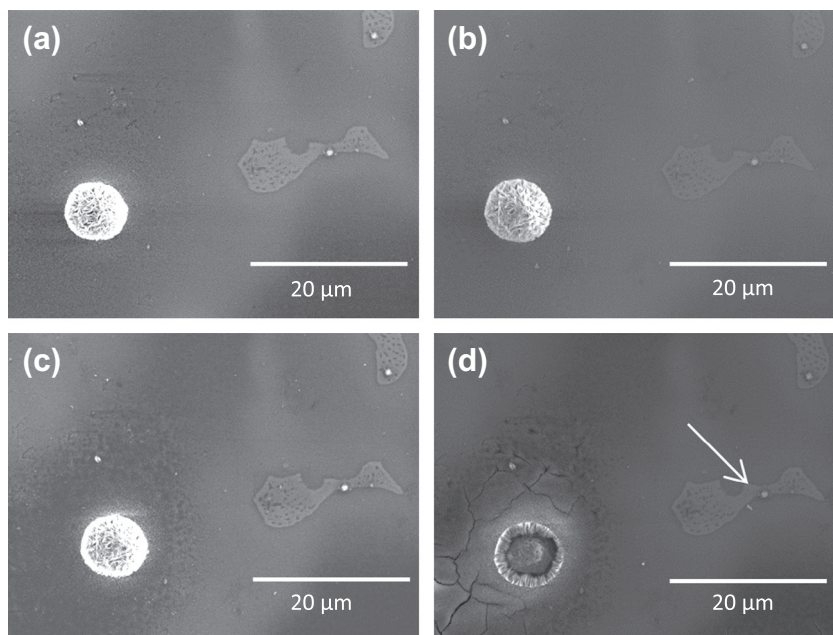


Fig. 5. SEM images (SE-10 kV) showing the progress of corrosion near an Al–Mn intermetallic from Fig. 2a) following (a) 24 h, (b) 48 h, (c) 72 h, and (d) 96 h of immersion in 1.6 wt% NaCl.

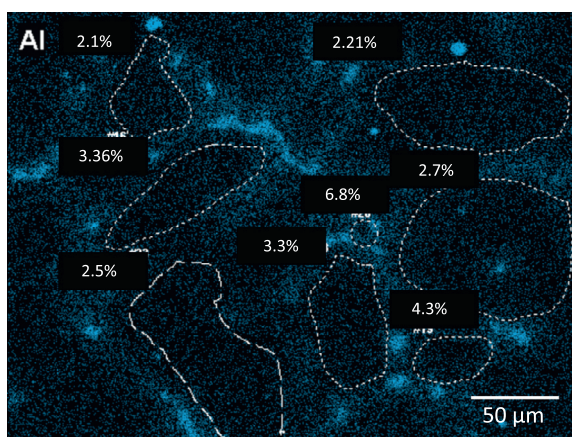


Fig. 6. Identification of the location of α -grains with their measured Al content on sand cast AM50 alloys using EDX mapping. Grains were numbered for further analysis shown in Fig. 8.

As discussed above, Al–Mn inclusions can increase the corrosion rate of individual α -grains, thus, it might be expected that a region with a clustering of inclusions could lead to the initiation of these major corrosion events, as observed in Figs. 10 and 11. Fig. 12a and e shows initial areas of the surface which eventually suffered major corrosion events. The positions of the major events are numbered in Fig. 12a, and with a red circle in Fig. 12e. While it was previously observed that Al–Mn intermetallics can accelerate corrosion of α -grains, no significant clustering of Al–Mn inclusions is observed at these sites. The dominant feature of these areas is the minimal presence of β -phase and the accompanying Al-rich network. These features suggest that it is areas with minimal Al content which are most susceptible to extensive corrosion propagation events, and a high population of local cathodes such as Al–Mn intermetallics does not play a substantial role. From Fig. 12d and h it can also be seen that corrosion does not expand outward following initiation but likely is propagating deeper into the alloy. This could lead to a major loss of structural integrity and eventual fallout of surface material, as observed in Fig. 10b.

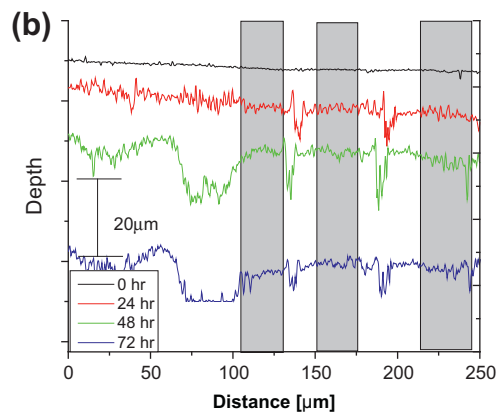
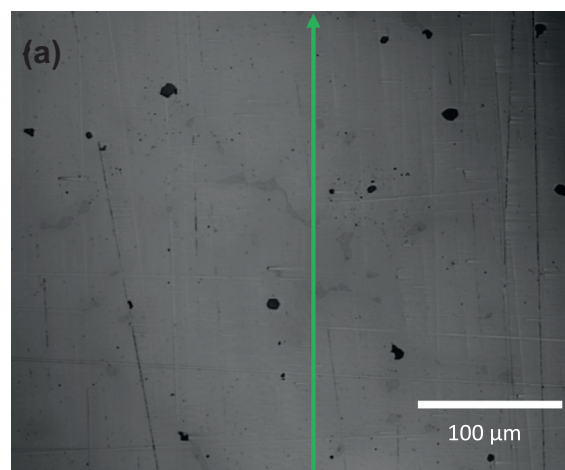


Fig. 7. (a) CLSM image showing the location of a depth profile line scan in green (bottom to top) and (b) the corresponding changes in depth throughout the successive immersions. The β -phases are highlighted in grey. (For interpretation of the references to color in this figure legend, the reader is referred to the web version of this article.)

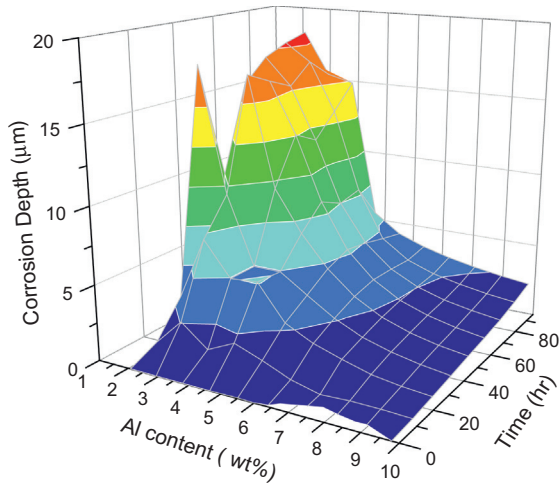


Fig. 8. The relationship between corrosion depth on α -grains and their Al content as a function of corrosion exposure time.

4. Discussion

By monitoring the same surface location through a series of aqueous immersion-dry cycles, the evolution of corrosion on sand cast AM50 alloys can be tracked on a microstructural scale. α -grains were continuously attacked throughout each aqueous exposure with corrosion rates dependent on Al content. Two cathodic microstructural features are present on the AM50 surface, the β -phase and Al–Mn intermetallics. Their function as cathodes is indicated by the accumulation of corrosion product at their location. Above the β -phase and in proximate regions, corrosion product still accumulated on the surface with a less dense corrosion product layer appearing over the β -phase. Based on additional

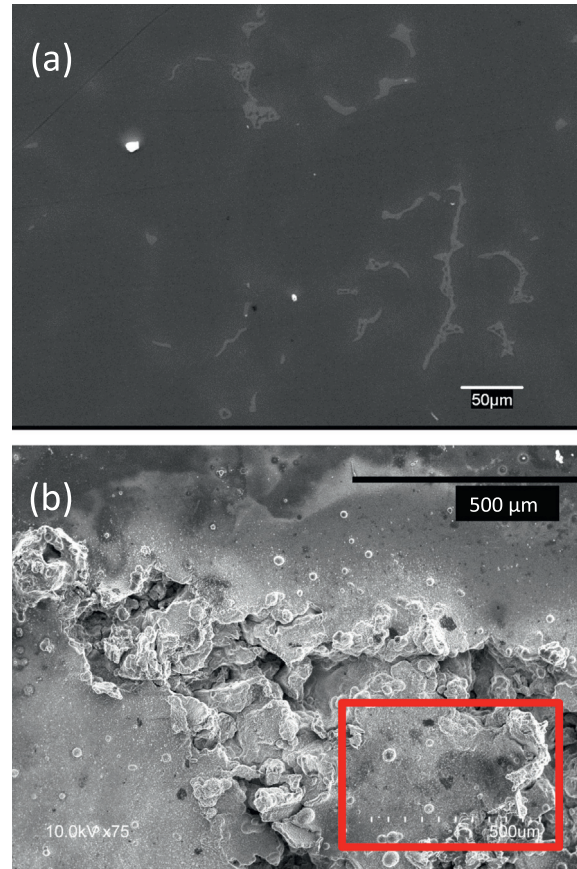


Fig. 10. (a) SEM micrograph (BSE) of an AOI on a sand cast AM50 alloy prior to corrosion, which was subsequently immersed for 24 h in 1.6 wt% NaCl; and (b) the AOI (red box) following the immersion surrounded by a major corrosion event. (For interpretation of the references to color in this figure legend, the reader is referred to the web version of this article.)

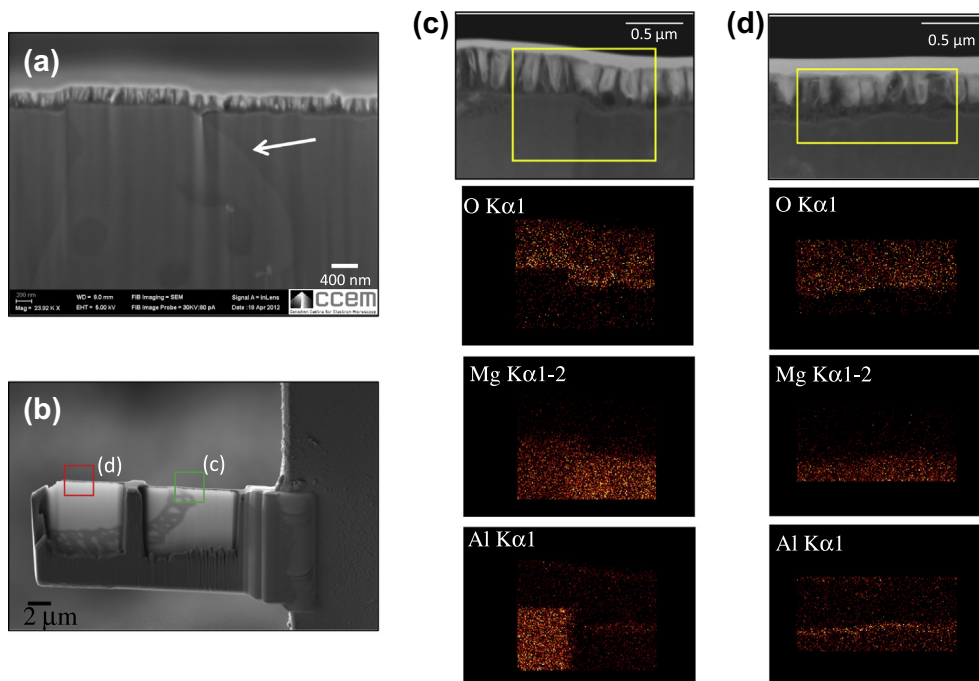


Fig. 9. (a) SEM image (in-lens-5 kV) of a FIB cross section of a β -phase region (marked with an arrow) including the adjacent only slightly corroded region after 96 h of corrosion; (b) SEM image (SE) of the TEM lamella of the selected region following lift out and thinning; (c) TEM images and the corresponding O, Mg and Al XEDS maps (300 kV) of the area marked in green; and (d) similar XEDS maps of the red area shown in (b). (For interpretation of the references to color in this figure legend, the reader is referred to the web version of this article.)

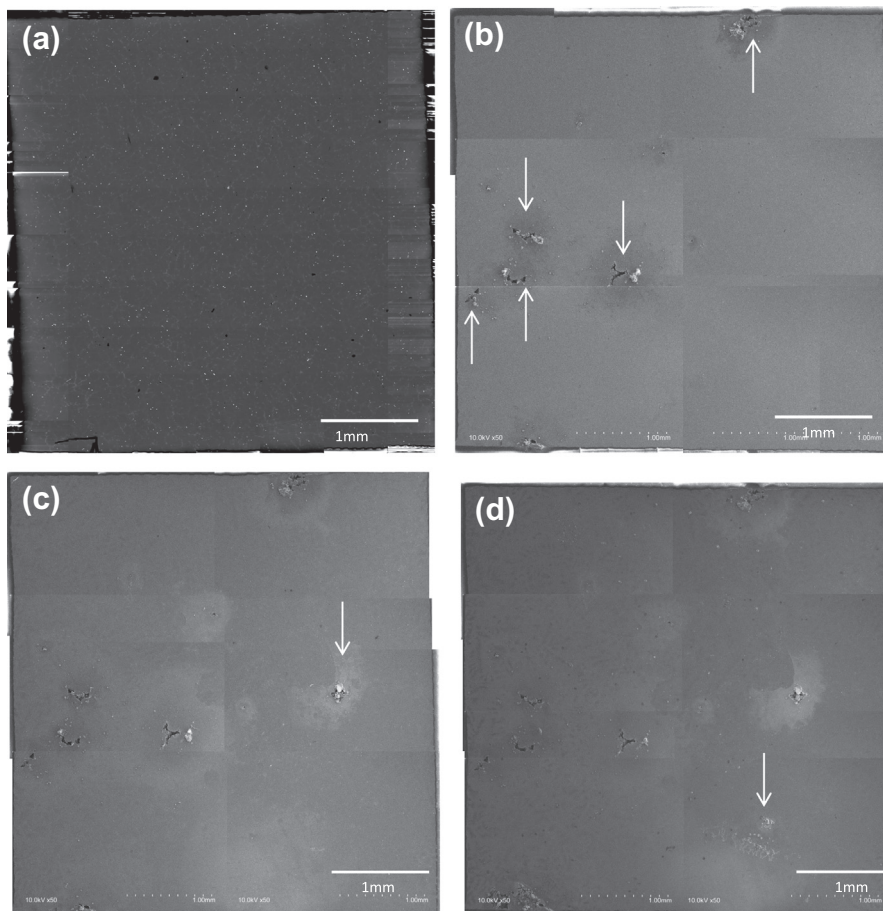


Fig. 11. (a) Montage SEM (BSE) image of a polished sand cast AM50 surface and SE images (10 kV) of the same area following (b) 2 h, (c) 3 h and (d) 4 h of immersion in 1.6 wt% NaCl. New damage sites are marked with arrows.

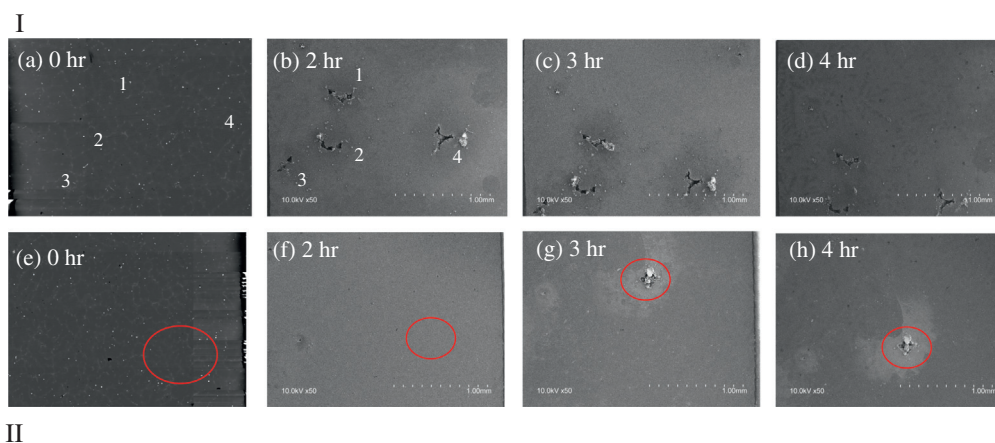


Fig. 12. SEM micrographs (SE-10 kV) of progression of areas which sustained major corrosion events: the corrosion damage is observed to penetrate into the alloy but not to spread across the surface.

studies, our analyses suggest this layer is $Mg(OH)_2$ and the difference in density above the β -phase is a purely morphological change [33]. Since the β -phase is expected to act as a cathode with respect to the α -grains in AM50 alloys, this change in density of the corrosion product on the β -phase compared to that on the α -phase may arise from its deposition at a location where water reduction to $H_{2(g)}$ leads to an increased pH [18]. The Al–Mn intermetallics, also suspected cathodic sites on the alloy, also accumulate corrosion product with immersion time forming a domed structure on

the surface. This dome is composed of an inner region of MgO and an outer region of $Mg(OH)_2$ [33] formed, presumably, in the alkaline environment prevailing at these cathodic sites. The presence of an intermetallic within an α -grain, acting as a local cathode, accelerates the corrosion rate of the individual grain irrespective of the Al content of that grain. This corrosion of the α -grains leaves behind a skeletal network of corrosion resistant regions that are rich in Al, which correspond to the Al-rich areas observed in XEDS maps. Analyses of cross-sections of these corrosion

resistant regions revealed an accumulated Al-layer between the corrosion product layer and the bulk alloy. That such an accumulation of Al improves the corrosion resistance, is consistent with observations in studies in which Al was enriched through surface modification [37,38] Although the chemical nature of this layer is known [33], the formation mechanism is yet to be determined.

These results show the importance of Al on the corrosion resistance of sand cast AM50 alloys, by lowering the rate of α -grain attack and generating a corrosion resistant region through surface accumulation. Its importance is emphasized by the accumulation of extensive corrosion damage over short exposure times at regions with minimal Al content. Localized cathodes (intermetallics) accelerate the corrosion of individual grains, but ultimately, it is a sparse distribution of Al that leads to the initiation of large corrosion events.

5. Conclusions

Microscopic and corrosion analyses on the same area of a sand cast AM50 alloy after intermittent solution immersions have provided a clear map of the evolution of corrosion damage and how it is affected by the galvanic effects of the microstructural constituents Using SEM/XEDS and CLSM to characterize the same area through a sequence of immersions the corrosion penetration depth was clearly related to local Al content. Al-rich β -phase and eutectic α -phase microstructures were most resistant to corrosion. In the latter case this was shown to be due to Al enrichment in a thin layer at the alloy/oxide interface. The alloy was found to be susceptible to major corrosion events in regions low in Al even after short (<2 h) immersion times. This shows that Al distribution is directly related to corrosion damage, and a more evened distribution of Al through microstructure manipulation may lead to enhanced corrosion properties. The procedure developed could be applied to a wide range of Mg alloys to investigate in more detail the effects of microstructure on corrosion resistance including the influences of grain size, β -phase distribution and results of surface treatments.

Acknowledgements

This work was funded by a Collaborative Research and Development grant supported by NSERC and General Motors and awarded to Western, McMaster and McGill Universities. We would like to acknowledge the staff at Surface Science Western, Integrated Microscopy at the Biotron Research Institute, and ZAPLab at Western University for their time and instrument use, and Janine Mauzeroll and her group at McGill University for the continuing collaboration in this project. MD and GAB acknowledge access to the microscopy facilities (FIB, TEM) at the Canadian Centre for Electron Microscopy, a National Facility supported by NSERC and McMaster University.

References

- [1] P. J. Blanchard, D.J. Hil, G.T. Bretz, R.C. McCune, Evaluation of corrosion protection methods for magnesium alloys in automotive applications, *Mag. Technol.* (2005) 463.
- [2] M.K. Kulecki, Magnesium and its alloys application in automotive industry, *Int. J. Adv. Manuf. Technol.* 39 (2008) 851–865.
- [3] G. Song, Recent progress in corrosion and protection of magnesium alloys, *Adv. Eng. Mater.* 7 (2005) 563–586.
- [4] K.B. Desphande, Effect of aluminum spacer on galvanic corrosion between magnesium and mild steel using numerical model and SVET experiments, *Corros. Sci.* 62 (2012) 184–191.
- [5] V.Y. Gertsman, L. Jian, S. Xu, J.P. Thomson, M. Sahoo, Microstructure and second-phase particles in low- and high-pressure die-cast magnesium alloy AM50, *Metall. Mater. Trans. A* 36A (2005) 1989–1997.
- [6] C. Blawert, D. Fechner, D. Hoche, V. Heitmann, W. Dietzel, K.U. Kainer, P. Zivanovic, C. Scharf, A. Ditze, J. Grobner, R. Schmid-Fetzer, Magnesium

secondary alloys: alloy design for magnesium alloys with improved tolerance limits against impurities, *Corros. Sci.* 52 (2010) 2452–2468.

- [7] D. Sachdeva, Insights into microstructure based corrosion mechanism of high pressure die cast AM50 alloy, *Corros. Sci.* 60 (2012) 18–31.
- [8] R.M. Wang, A. Eliezer, E.M. Gutman, An investigation on the microstructure of an AM50 magnesium alloy, *Mater. Sci. Eng. A* A355 (2003) 201–207.
- [9] C. Op't Hoogm, N. Birbilis, Y. Estrin, Corrosion of pure Mg as a function of grain size and processing route, *Adv. Eng. Mater.* 10 (2008) 579–582.
- [10] J. Liao, M. Hotta, S. Motoda, T. Shinohara, Atmospheric corrosion of two field-exposed AZ31B magnesium alloys with different grain size, *Corros. Sci.* 71 (2013) 53–61.
- [11] F. Andreatta, I. Apachitei, A.A. Kondentsov, J. Dzwonczyk, J. Duszczyk, Volta potential of second phase particles in extruded AZ80 magnesium alloy, *Electrochim. Acta* 51 (2006) 3551–3557.
- [12] J. Liao, M. Hotta, N. Yamamoto, Corrosion behaviour of fine-grained AZ31B magnesium alloy, *Corros. Sci.* 61 (2012) 208–214.
- [13] D. Orlov, K.D. Ralston, N. Birbilis, Y. Estrin, Enhanced corrosion resistance of Mg alloy ZK60 by integrated extrusion and equal channel angular pressing, *Acta Mater.* 59 (2011) 6176–6186.
- [14] M. Laleh, F. Kargar, Effect of surface nanocrystallization on the microstructural and corrosion characteristics of AZ91D magnesium alloy, *J. Alloys Compd.* 509 (2011) 9150–9156.
- [15] D. Song, A.B. Ma, J.H. Jiang, P.H. Lin, D.H. Yang, J.F. Fan, Corrosion behaviour of bulk ultra-fine grained AZ91D magnesium alloy fabricated by equal-channel angular pressing, *Corros. Sci.* 53 (2011) 362–373.
- [16] N.N. Aung, W. Zhou, Effect of grain size and twins on corrosion behaviour of AZ31B magnesium alloy, *Corros. Sci.* 52 (2010) 589–594.
- [17] K.D. Ralston, N. Birbilis, Effect of grain size on corrosion: a review, *Corrosion* 66 (2010) 1–13.
- [18] Y. Ma, J. Zhang, M. Yang, Research on microstructure and alloy phases of AM50 magnesium alloy, *J. Alloys Compd.* 470 (2009) 515–521.
- [19] G. Song, A. Atrens, Corrosion mechanisms of magnesium alloys, *Adv. Eng. Mater.* 1 (1999) 11–33.
- [20] R. Ambat, N.N. Aung, W. Zhou, Evaluation of microstructural effects on corrosion behaviour of AZ91D magnesium alloy, *Corros. Sci.* 42 (2000) 1433–1455.
- [21] T. Zhang, Y. Shao, G. Meng, Z. Cui, F. Wang, Corrosion of hot extrusion AZ91 magnesium alloy: I-relation between the microstructure and corrosion behaviour, *Corros. Sci.* 53 (2011) 1960–1968.
- [22] M. Zhao, M. Liu, G. Song, A. Atrens, Influence of the β -phase morphology on the corrosion of the Mg alloy AZ91, *Corros. Sci.* 50 (2008) 1939–1953.
- [23] C. Lih, M.Z.M. Zamzuri, S. Norbahyah, K.A. Ismail, M.N.B. Derman, S. Ilias, Effect of heat treatment on microstructure and corrosion behaviour of AZ91D magnesium alloy, *Adv. Mater. Res.* 685 (2013) 102–106.
- [24] J.H. Nordlien, K. Nisancioglu, S. Ono, N. Masuko, Morphology and structure of water-formed oxides on ternary MgAl Alloys, *J. Electrochem. Soc.* 144 (1997) 461–466.
- [25] R. Lindstrom, J.E. Svensson, L.G. Johansson, The influence of carbon dioxide on the atmospheric corrosion of some magnesium alloys in the presence of NaCl, *J. Electrochem. Soc.* 149 (2002) B103–B107.
- [26] P. Volovitch, M. Serdechnova, K. Ogle, Aqueous corrosion of Mg–Al binary alloys: roles of Al and Mg, *Corrosion* 68 (2012) 557–570.
- [27] M. Jonsson, D. Persson, The influence of the microstructure on the atmospheric corrosion behaviour of magnesium alloys AZ91D and AM50, *Corros. Sci.* 52 (2010) 1077–1085.
- [28] M. Jonsson, D. Persson, R. Gubner, The initial steps of atmospheric corrosion on magnesium alloy AZ91D, *J. Electrochem. Soc.* 154 (2007) C684–C691.
- [29] Y. Yang, H. Wu, Effect of current density on corrosion resistance of micro-arc coatings on magnesium alloy, *Trans. Nonferrous Met. Soc. China* 20 (2010) s688–s692.
- [30] L.F. Garfias-Mesias, M. Alodan, P.I. James, W.H. Smyrl, Determination of precursor sites for pitting corrosion on polycrystalline titanium by using different techniques, *J. Electrochem. Soc.* 145 (1998) 2005–2010.
- [31] O. Schneider, G.O. Ilevbare, J.R. Scully, R.G. Kelly, Confocal laser scanning microscopy as a tool for in situ monitoring of corrosion underneath organic coatings, *Electrochem. Solid State Lett.* 4 (2001) B35–B38.
- [32] G. Song, A. Atrens, M. Dargusch, Influence of microstructure on the corrosion of diecast AZ91D, *Corros. Sci.* 41 (1999) 249–27.
- [33] M. Danaie, R.M. Asmussen, P. Jakupi, D.W. Shoesmith, G.A. Botton, Site-specific microstructure characterization of the surface layer in a sand-cast magnesium–aluminum alloy (AM50) corroded in an aqueous NaCl solution, *Corros. Sci.*, submitted for publication 2013.
- [34] S. Mathieu, C. Rapin, J. Steinmetz, A corrosion study on the main constituent phases of AZ91 magnesium alloys, *Corros. Sci.* 45 (2003) 2741–2755.
- [35] A. Pardo, M.C. Merino, A.E. Coy, R. Arrabal, F. Viejo, E. Matykina, Effect of Mo and Mn additions on the corrosion behaviour of Al Si 304 and 316 stainless steels in H₂SO₄, *Corros. Sci.* 50 (2008) 823–834.
- [36] R.C. Phillips, J.R. Kish, Nature of surface film on matrix phase of Mg alloy AZ80 formed in water, *Corrosion* (2013). in-press (<http://dx.doi.org/10.5006/0938>).
- [37] Y.C. Guan, W. Zhou, H.Y. Zheng, Effect of laser surface melting on corrosion behaviour of AZ91 Mg alloy in simulated-modified body fluid, *J. Appl. Electrochem.* 39 (2009) 1457–1464.
- [38] A.E. Coy, F. Viejo, F.J. Garcia-Garcia, Z. Liu, P. Skeldon, G.E. Thompson, Effect of excimer laser surface melting on the microstructure and corrosion performance of the die cast AZ91D magnesium alloy, *Corros. Sci.* 52 (2010) 387–397.